EuroSun2026

DEVELOPMENT OF AN OPEN-SOURCE SOLAR CADASTRE IN QGIS

Paula Felten[1], Florian Betz[2], Mathias Ehrenwirth[1,*]

[1]Technische Hochschule Nürnberg Georg Simon Ohm, Institute for Energy and Building, Nürnberg (Germany)
[2]Universität Würzburg, Earth Observation Research Cluster, Würzburg (Germany)

[*]Corresponding author: `mathias.ehrenwirth@th-nuernberg.de`

Summary

This study addresses the need for scalable urban energy planning by developing a comprehensive workflow to assess rooftop photovoltaic potential using the open-source geographic information system *QGIS* and open data. Applied to the case of *Nuremberg*, Germany, the methodology derives homogeneous roof areas from LiDAR and building footprint data, models annual solar irradiation under real-sky conditions using the *GRASS GIS* module `r.sun.insoltime`, and calculates temperature-adjusted PV yields. Differentiating itself from standard literature, the approach integrates a modular layout algorithm to determine installable PV capacities alongside a multi-criteria scoring matrix for spatial suitability prioritisation. Results show orientation-specific annual yields ranging from $132\,\mathrm{kW\,h/(m^2\,a)}$ for east-facing roofs to $179\,\mathrm{kW\,h/(m^2\,a)}$ for south-facing roofs, with module coverage factors between 0.38 and 0.45 depending on roof type. Overall, the results confirm that the derived geometric potentials, modelled irradiation, and estimated yields align robustly with existing benchmarks, providing a transparent, transferable, and data-driven tool for decentralised renewable infrastructure development and strategic municipal PV planning.

Keywords: Solar cadastre, PV potential, GIS, open-source, open data, opportunity mapping

Field of application for the findings: PV expansion planning and decentralised infrastructure development

Addressed audience: Local authorities, planners, private building owners

1. Introduction

Photovoltaic power generation has become a central component of Germany's transition to a low-carbon energy system. As the second-largest source of net electricity generation after wind power, PV has contributed to more than halving the CO_2-equivalent emission factor of the German electricity mix since 1990 (Fraunhofer-Institut für Solare Energiesysteme ISE, 2025; Wirth, 2025, p. 46). Its role in reducing climate-related risks is also reflected in Section 4 of the German Renewable Energy Sources Act, which sets targets for installed PV capacity of 215 GWp by 2030 and 400 GWp by 2040 (EEG, 2025).

As shown in Figure 1, meeting these targets will require continued growth in PV capacity. This calls for a systematic assessment of technically suitable PV areas and their prioritisation based on energy-system relevance and techno-economic performance. According to Wirth (2025, p. 32), less than 10 % of the available rooftop potential has been utilised to date, showing substantial remaining potential. Furthermore, rooftops are particularly suitable for PV deployment, as they are underutilised surfaces, avoid competition with agricultural land and are typically located close to electricity demand.

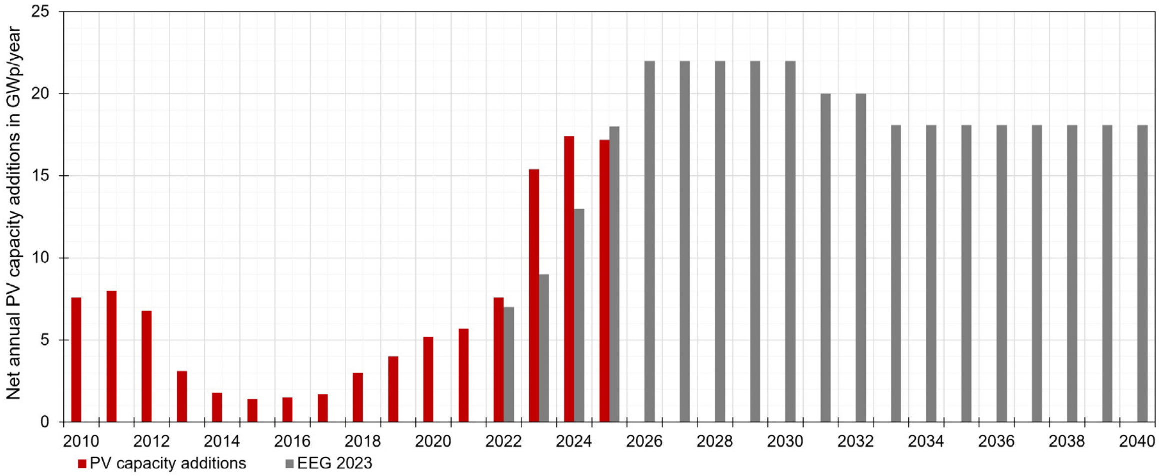

Fig. 1: Annual net PV additions in Germany and expansion pathway according to the Renewable Energy Sources Act 2023 (EEG, 2025). Own illustration based on Wirth (2025, p. 6).

The scientific literature provides a broad range of approaches for assessing rooftop PV potential, including individual steps such as roof detection, irradiation modelling, shading analysis, technical filtering and yield estimation. Methods based on geographic information systems (GIS) are widely used in this field, but differ in their level of complexity. Simplified two-dimensional workflows can use empirically derived correction factors to compensate for missing information, enabling computationally efficient PV-potential estimation over large study areas (cf. Uhl and Arnold, 2013). More detailed three-dimensional or LiDAR-based methods derive roof geometry directly from high-resolution elevation data, allowing roof slope, orientation and shading to be represented under the specific local conditions (Adjiski et al., 2023; Cenky et al., 2024; Ludwig, 2015; Tro-Cabrera et al., 2025). These approaches generally provide higher geometric accuracy, but also demand a higher level of data processing.

Ludwig (2015) developed a transparent GIS-based workflow for automated rooftop solar potential assessment using high-resolution LiDAR data. A multi-thresholding approach enables precise identification of suitable roof segments. Adjiski et al. (2023) analysed rooftop PV potential in the *Skopje* region using high-resolution geodata. Cenky et al. (2024) demonstrated that urban rooftop PV potential can be assessed using open-source software and public geodata, highlighting the relevance of reproducible and accessible workflows. Tro-Cabrera et al. (2025) extended GIS-based PV assessment by integrating technical and energetic indicators, including temperature-adjusted yield estimation, module efficiency degradation and the energy return on energy investment (EROI). Hou et al. (2025) further emphasised the importance of atmospheric inputs for urban solar irradiation modelling, showing that clouds, aerosols and localised shading can substantially reduce rooftop irradiation relative to idealised clear-sky conditions.

Solar cadastres present the results of these methodological approaches to end users through intuitive digital maps. The availability of solar cadastres across Germany highlights the importance of accessible information on PV suitability and economic viability for achieving PV expansion targets. However, a comparative overview by Bieda and Cienciała (2021) shows that existing approaches lack a common methodological standard. Solar cadastres differ substantially in terms of input data, methodological design, spatial detail, and available functionalities, even within the same country.

Building on these approaches, the study developed a transparent and fully open-source workflow for rooftop PV potential assessment integrating roof-segment extraction, irradiation modelling, technical filtering, yield estimation and a simple module-placement algorithm. It further translates the resulting potential estimates into a prioritisation map intended to support municipal planning. The approach is designed to be reproducible and transferable to other municipalities where comparable input data are available.

2. Method

2.1 Case study

The study area is a 1 km × 1 km grid cell within the inner city of *Nuremberg*, Germany. The area contains a dense mix of residential, commercial, and mixed-use buildings with a variety of roof types, including pitched roofs oriented in all cardinal directions and large flat-roof structures. The reference year for all time-series calculations is 2024. The results of the developed cadastre are validated against reference studies and the official solar cadastre of the City of *Nuremberg*.

2.2 Tools and input data

The solar cadastre was developed entirely within the open-source geographic information system *QGIS*. The main processing steps included raster and vector processing using the *Geospatial Data Abstraction Library* (GDAL) and native processing algorithms, solar irradiation analysis using *Geographic Resources Analysis Support System* (GRASS GIS) tools, and workflow automation via the Python interface. The workflow relies exclusively on openly available geospatial datasets. Table 1 summarises the input data and their respective functions within the workflow.

Tab. 1: Overview of the input datasets and their integration into the workflow. LDBV datasets: Bayerische Vermessungsverwaltung – https://www.geodaten.bayern.de (data modified), CC BY 4.0.

No.	Input dataset	Source	Data type	Function in the workflow
1	LiDAR point cloud	Bavarian Agency for Digitisation, High-Speed Internet and Surveying (LDBV)	LAZ point cloud	Derivation of building-specific elevation information
2	Building footprints	LDBV	SHAPE	Spatial localisation of buildings and assignment of individual roof segments
3	Albedo data	NASA ECOSTRESS	TIF	Representation of ground-reflected solar radiation in the irradiation analysis
4	Linke turbidity factor	Bourges formula	–	Representation of atmospheric turbidity in the solar irradiation analysis
5	Solar radiation data	German Weather Service (DWD)	ASCII Raster	Generation of clear-sky index rasters to account for cloud-cover effects in the solar irradiation analysis
6	Digital Terrain Model (DTM)	LDBV	GeoTIFF	Reference surface for calculating horizontal solar irradiation
7	Temperature data	DWD	TXT	Estimation of PV cell temperature and associated temperature-related performance losses
8	Existing PV installations	Energie-Atlas Bayern	KML	Identification of roof areas already occupied by existing PV installations
9	ATKIS Basis-DLM land-use layer	LDBV	SHAPE	Approximation of local electricity-demand potential based on land use
10	Heat and cooling demand density map	Citiwatts	TIF	Integration of spatial heating and cooling demand indicators
11	Monument protection data	Bavarian State Office for Monument Protection (BLfD)	WMS/Vector data	Identification of heritage-protected areas and potential approval restrictions; for informational purposes only

2.3 Workflow and data preparation

The overall workflow follows a sequential processing chain from raw geodata to a spatial priority map. Figure 2 provides a simplified overview of the main steps and data flows.

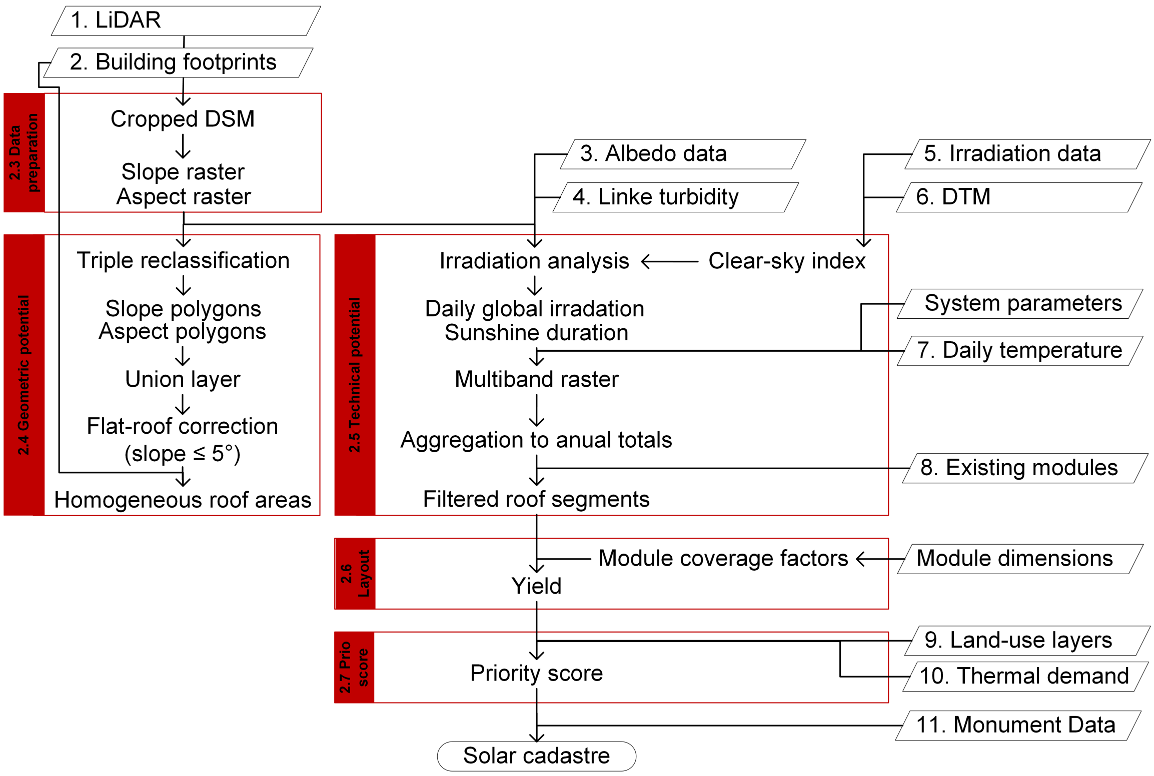

Fig. 2: Simplified overview of the GIS-based workflow. Input datasets and user-defined parameters are shown as parallelograms, while the larger red-outlined blocks correspond to the methodological sections described in the following chapters. Arrows indicate the processing sequence from data preparation and roof segmentation to irradiation modelling, PV yield estimation and the final priority-based solar cadastre (rounded rectangle).

First, the input datasets are harmonised in the coordinate reference system ETRS89 / UTM zone 32N (EPSG:25832) and prepared for the analysis. The LiDAR point cloud is converted into a Digital Surface Model (DSM) using the `Triangulation` module and clipped to the building outlines. The DSM is then used to generate slope and aspect rasters with the *GRASS GIS* module `r.slope.aspect`.

2.4 Geometric potential

Roof segmentation is carried out using a multi-thresholding approach adapted from Ludwig (2015, p. 69 ff.). The method identifies homogeneous roof areas based on similar slope and aspect values which are then reclassified into broader value classes. Roof structures such as chimneys, technical installations, and local geometric variations are filtered out based on their distinct characteristics, preventing overestimation of the available roof area.

As shown in Figure 3, the classification scheme applied in the first segmentation run divides slope values into eleven classes and aspect values into four orientation classes. Raster cells assigned to comparable classes are aggregated into vector polygons representing individual roof segments.

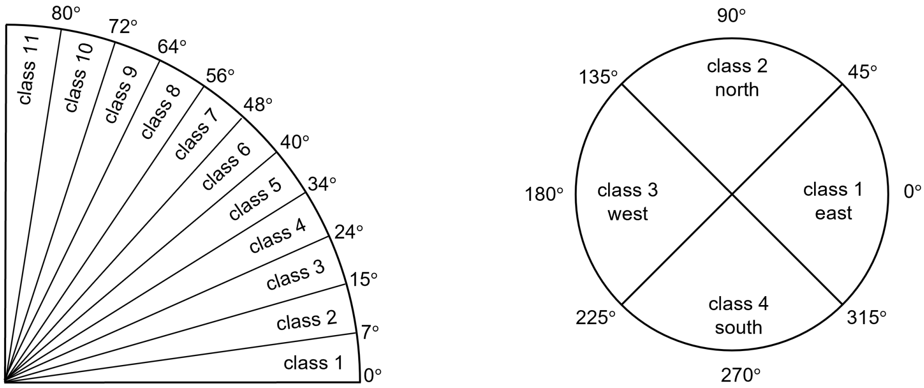

Fig. 3: Classification of slope and aspect values for the first thresholding round. Own illustration based on Adjiski et al. (2023, p. 192); classification scheme based on Ludwig (2015, p. 72).

The segmentation is refined across three thresholding passes. In each pass, the median slope and aspect values are calculated for the polygonised segments and then rasterised again to provide a generalised input for the next reclassification step. The class boundaries are slightly adjusted, allowing adjacent raster cells to merge into larger, coherent polygons. Figure 4 illustrates the progression of slope and aspect segmentation across the three thresholding passes.

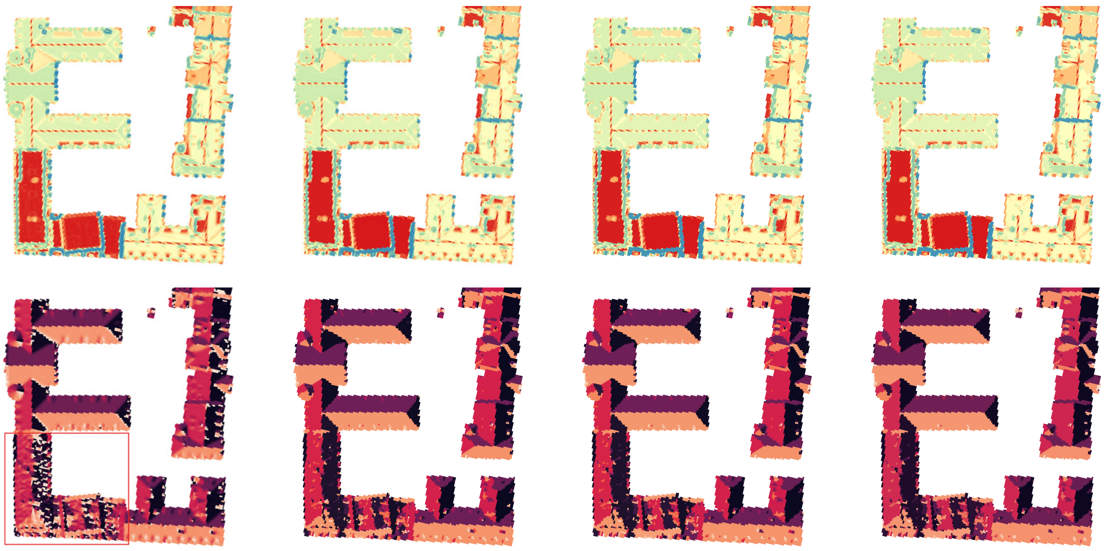

Fig. 4: Three-step thresholding workflow. The top row illustrates the slope classification, while the bottom row shows the aspect classification, each starting from the respective primary raster layer.

The highlighted area in Figure 4 illustrates a limitation of the method for flat roofs. Since a horizontal surface has no geometrically meaningful orientation, aspect values produce strongly fragmented polygons in the aspect layer. Translating this fragmentation into the union layer would result in an artificial subdivision of flat-roof areas into numerous small polygons. Accordingly, roof segments with a slope of $\leq 5°$ are classified as flat roofs (adapted from DIN Deutsches Institut für Normung e.V., 2024). Their aspect values are overwritten with a uniform placeholder value of 361, ensuring that flat roofs are treated as a single orientation class.

The final roof polygons are overlaid with the building footprints using a union operation, allowing each roof segment to be assigned to a specific building. The intermediate layer is shown in Figure 6. For all roof segments, the roof surface area is approximated by dividing the two-dimensional projected area by the cosine of the respective slope angle.

2.5 Technical potential

The technical potential is assessed using the *GRASS GIS* module `r.sun.insoltime`. The simulation is based on the DSM as well as the derived slope and aspect rasters. To represent realistic atmospheric conditions, the model integrates high-resolution meteorological input data, including monthly mean albedo rasters, daily Linke turbidity values, and clear-sky index rasters for direct and diffuse radiation.

Monthly mean albedo rasters are derived from NASA ECOSTRESS albedo scenes between 2018 and 2025 (Hook et al., 2023). Scenes with a spatially uniform albedo value of 0.3, identified as implausible sensor artefacts, are excluded, as are individual pixels with an uncertainty flag of 0.3 or higher. Daily Linke turbidity values are calculated using the Bourges empirical formula with coefficients for the Continental turbidity zone ($T_0 = 3.90, u = -0.76, v = -0.0032$) (Wellner and Kayser, 2007, p. 39). Clear-sky index rasters for direct and diffuse radiation are derived following Hofierka and Šúri (2002, p. 13) as the ratio of observed irradiation to the corresponding `r.sun.insoltime` clear-sky estimate, using the DWD monthly direct and diffuse radiation products (DWD Climate Data Center (CDC), 2025a,b). The resulting monthly clear-sky indices are applied to all simulation days within the respective month. Terrain shadowing is enabled to account for shading by buildings and topography. Following the recommendations in the *GRASS GIS* documentation, shadow calculations use a distance step of 1.0 and a time step of 0.05 (Hofierka et al., 2025). The simulation is run for all days of 2024, producing raster outputs of global irradiation and sunshine duration that are subsequently aggregated to the roof segment level.

The global irradiation values from `r.sun.insoltime` are converted into specific PV yield following the approach of Tro-Cabrera et al. (2025):

$$E = \eta \cdot PR_\mathrm{T} \cdot GI \tag{1}$$

where

E	daily specific PV yield in $\mathrm{Wh\,m^{-2}}$,
η	module efficiency,
PR_T	temperature-adjusted performance ratio,
GI	daily global irradiation in $\mathrm{Wh\,m^{-2}}$.

The default module efficiency is set to 22.54 %, based on the market-weighted average of crystalline silicon and CdTe module efficiencies (own calculation based on Philipps and Warmuth, 2025, p. 33; Wirth, 2025, p. 79). Temperature-related losses are considered using a temperature-adjusted performance ratio:

$$PR_\mathrm{T} = PR \cdot [1 + \gamma \cdot (T_\mathrm{c} - T_\mathrm{STC})] \tag{2}$$

where

PR	reference performance ratio,
γ	temperature coefficient,
T_c	cell temperature in °C,
T_STC	standard test condition temperature of 25 °C.

The reference performance ratio is set to 84 % by default. This value lies within the typical range of 80 % to 90 % reported for modern PV systems by Fraunhofer ISE (Philipps and Warmuth, 2025, p. 6). The default temperature coefficient is set to $\gamma = -0.004\ \mathrm{K^{-1}}$.

The cell temperature is estimated as

$$T_\mathrm{c} = T_\mathrm{air} + GI \cdot \frac{NOCT - 20\ ^\circ\mathrm{C}}{800\ \mathrm{W\,m^{-2}} \cdot t_\mathrm{is}} \tag{3}$$

where

T_air	ambient air temperature in °C,
GI	daily global irradiation in $\mathrm{Wh\,m^{-2}}$,
t_is	sunshine duration in h,
$NOCT$	nominal operating cell temperature in °C.

The default nominal operating cell temperature is set to $NOCT = 45.0\ ^\circ\mathrm{C}$. PR, γ and $NOCT$ are user-defined parameters and can be adjusted to represent different PV module characteristics.

The ambient air temperature is obtained from daily DWD station observations (DWD Climate Data Center (CDC), 2024), while GI and t_{is} are derived from `r.sun.insoltime`.

Prior to yield aggregation, unsuitable roof segments are excluded following literature-based suitability criteria. A minimum segment area of $10\,\text{m}^2$ is applied, following Ludwig (2015, p. 90), and is also consistent with comparable minimum-area assumptions reported by Adjiski et al. (2023, p. 194) and McGhee et al. (2024, p. 13). This threshold removes small roof fragments as well as areas with negligible energetic contribution. North-facing roofs are excluded based on their limited PV potential, consistent with Uhl and Arnold (2013, p. 11). Roof inclinations exceeding 60° are removed in accordance with Adjiski et al. (2023, p. 194) and Cenky et al. (2024, p. 3972). Existing registered PV installations are excluded using data obtained from Energie-Atlas Bayern (Bayerisches Landesamt für Umwelt, 2025). Solar suitability is considered through a minimum annual global irradiation of $890\,\text{kW h}/(\text{m}^2\,\text{a})$, corresponding to approximately 80 % of the German mean annual global irradiation of $1{,}113\,\text{kW h}/\text{m}^2$ reported for 2024 by Püschel (2025).

2.6 Module layout

The usable module area is estimated using a simplified grid-based placement approach. The method differentiates between pitched and flat roofs. For pitched roofs, the module tilt is assumed to follow the roof pitch. For flat roofs, the user can define the module tilt and choose either a south-facing or an east-west arrangement. In south-facing flat-roof systems, row spacing is adjusted using a shadow-distance calculation to reduce mutual shading.

Because the roof geometries are represented as two-dimensional polygons, the module dimensions are projected onto the horizontal plane according to the selected tilt angle. Based on these projected dimensions and the defined spacing assumptions, a rectangular module grid is generated. The grid is then rotated according to the roof or module orientation and shifted iteratively across the roof geometry. For each tested position, the number of module cells fully contained within the roof polygon is counted. The position with the highest number of valid modules is selected as the best layout for the respective roof.

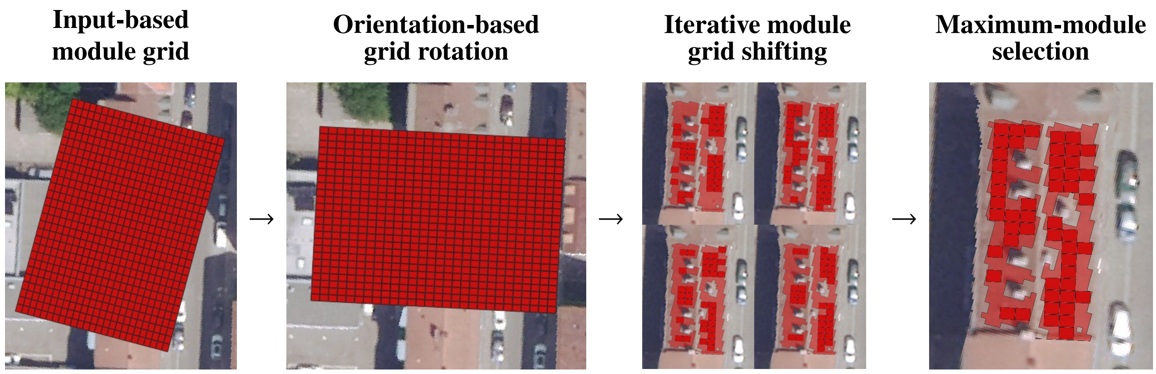

Fig. 5: Illustrative module layout for a pitched roof, showing the grid rotation, grid shifting, and maximum-module selection procedure. Background: Bayerische Vermessungsverwaltung – https://www.geodaten.bayern.de (data modified), CC BY 4.0.

The procedure shown in Figure 5 is first applied to a random sample of roofs. For each sampled roof, the fitted module area is calculated from the number of placed modules, the projected grid-cell area and a shading reduction factor. The sampled roofs are then grouped by orientation class, including east-, south-, west-facing and flat roofs. For each class, a module coverage factor is derived as the ratio between the total fitted module area and the total roof area of all sampled roofs in that class. In the final potential assessment, the roof-specific energy value is multiplied by the roof area and the corresponding module coverage factor. The resulting yield estimates, along with geometric and irradiation data, are stored as attributes of the roof-segment polygons. The total PV potential of the study area is obtained by summing the annual yields of all suitable roof segments within a selected area.

2.7 Priority score

The priority score is calculated to support strategic planning by combining three individual scores into a single indicator and applying an EROI-based scaling factor, allowing different criteria to be considered when assessing the suitability and priority of an area:

$$S_{\text{final}} = \left(0.7 \cdot S_{\text{yield}} + 0.25 \cdot S_{\text{elec}} + 0.05 \cdot S_{\text{HC}}\right) \cdot S_{\text{EROI}} \tag{4}$$

where

S_{final} final priority score,
S_{yield} indicator of the PV electricity yield per unit area,
S_{elec} indicator of the land-use-based electricity demand,
S_{HC} indicator of heating and cooling demand density,
S_{EROI} EROI-based scaling factor.

The weighting factors of 0.70, 0.25 and 0.05 were selected for the present case study to place the strongest emphasis on PV yield. They are user-defined and can be adjusted according to the objectives and priorities of the respective application.

The PV yield is normalised to a scale from 0 to 100 using the minimum and maximum yield values within the study area.

Local electricity demand is considered using land-use information from the *ATKIS Basis-DLM*. Higher scores are assigned to industrial and commercial areas (100), followed by areas of special functional use (80), mixed-use areas (60) and residential areas (40). The score of the dominant overlapping land-use category is assigned to each roof segment. This ranking reflects typical differences in electricity demand and self-consumption potential and can be adjusted.

Heat and cooling demand density maps from the *Citiwatts* project are included as an indicator of energy demand (OpenGIS4ET Team, 2025). Areas with a higher heating or cooling demand density are assumed to have a higher likelihood of electrification through technologies such as heat pumps. The indicator is therefore a weakly weighted proxy for future local energy demand and is normalised to a scale from 0 to 100 using the minimum and maximum heating or cooling demand within the study area.

The EROI-based scaling factor rewards roof segments with higher energetic quality and assigned as

$$S_{\text{EROI}} = \begin{cases} 0.95, & EROI < 9, \\ 1.00, & 9 \leq EROI < 12, \\ 1.05, & 12 \leq EROI < 15, \\ 1.08, & EROI \geq 15. \end{cases} \tag{5}$$

The EROI itself is calculated following Tro-Cabrera et al. (2025):

$$EROI = \frac{LT \cdot E_{\text{PV}}}{E_{\text{input}} \cdot g_{\text{syst}}} \tag{6}$$

where

LT assumed system lifetime in a,
E_{PV} annual PV production per unit area in $\text{kWh}\,\text{m}^{-2}\,\text{a}^{-1}$,
E_{input} life-cycle energy input of the system in $\text{kWh}\,\text{m}^{-2}$,
g_{syst} system quality factor.

A system lifetime of 30 years is assumed. This is consistent with common PV module lifetimes of 25–30 years (Wirth, 2025, p. 50) and slightly below the 33-year average lifetime used by the Swiss Federal Office of Energy (Hostettler, 2025, p. 23). The quality factor is set to 0.56, based on the primary energy factor of 1.8 for grid electricity according to Annex 4 of the German Building Energy Act (GEG, 2024). The market-weighted life-cycle energy input is set to $766\,\text{kW}\,\text{h}/\text{m}^2$, based on module-specific energy inputs reported by Bani Salim et al. (2018) and the market-share weighting Wirth (2025, p. 79).

3. Results

The developed solar cadastre was evaluated against the official *Nuremberg* solar cadastre. Furthermore, the results of the methodology were benchmarked against findings reported in previous studies.

3.1 Validation against the Nuremberg solar cadastre

Both approaches identify a broadly similar set of suitable roof segments. Differences mainly concern flat roofs and small areas: the *Nuremberg* cadastre excludes areas with a shading fraction above 80 %, whereas the developed workflow removes homogeneous roof sub-areas below 10 m^2 (IP SYSCON and Referat für Umwelt und Gesundheit, Stadt Nürnberg, 2023). Usable irradiation is slightly lower in the developed cadastre but shows a comparable distribution. The largest deviations occur for flat roofs, indicating the sensitivity of the technical potential to assumptions on usable area and module layout.

3.2 Methodology outputs

Across the complete study area, 3,179 of 241,628 analysed roof segments satisfy all suitability criteria. Figure 6 illustrates the effect of the filtering procedure.

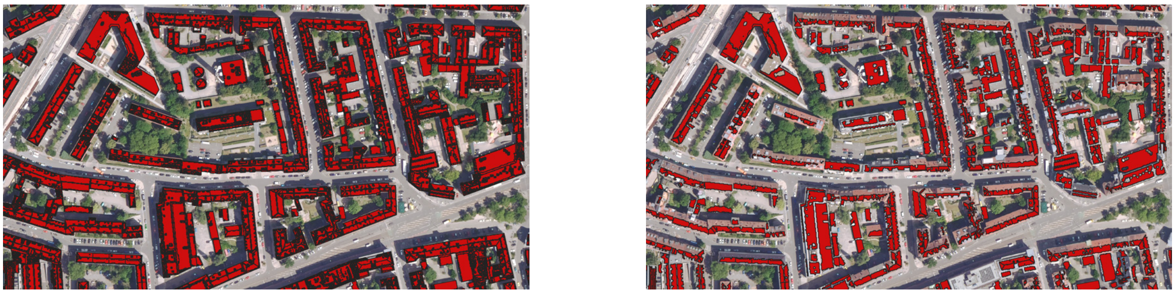

Fig. 6: Homogeneous roof sub-areas: unfiltered result *(left)* and filtered result after applying all suitability criteria *(right)*. Background: Bayerische Vermessungsverwaltung – https://www.geodaten.bayern.de (data modified), CC BY 4.0.

3.2.1 Module coverage factors

For 500 randomly selected suitable roof segments, the derived module coverage factors range from 0.383 for flat roofs to 0.453 for west-facing roofs; east- and south-facing roofs yield 0.407 and 0.404, respectively. The resulting 38 % to 45 % range agrees with approximately 40 % reported by Koch et al. (2022) and 45 % by Sun et al. (2022), while the manually optimised layouts of Anderegg et al. (2022) achieve higher shares of 63 % for pitched and 53 % for flat roofs.

3.2.2 PV yield

The specific annual yields follow the expected orientation dependence, with south-facing roofs achieving the highest values, followed by west- and east-facing roofs (Table 2). The annual values of 132 kWh/m^2 to 179 kWh/m^2 are comparable to the 138.42 kWh/m^2 to 157 kWh/m^2 reported for North Rhine-Westphalia (Landesamt für Natur, Umwelt und Verbraucherschutz Nordrhein-Westfalen, 2013).

Tab. 2: Average specific yields categorised by orientation.

Category	Specific daily yield in Wh/m^2	Specific annual yield in kWh/m^2
South	489.88	178.80
West	414.37	151.24
East	362.21	132.21

3.2.3 Solar cadastre

The final solar cadastre assigns a priority score from 0 to 100 to each suitable roof segment and overlays heritage-protected buildings and ensembles to indicate potential approval restrictions (Figure 7).

Fig. 7: Final solar cadastre showing the priority score for suitable roof segments and overlaid heritage-protected areas. Background: Bayerische Vermessungsverwaltung – https://www.geodaten.bayern.de (data modified), CC BY 4.0.

4. Discussion

Using open data and *QGIS*-based processing, the approach is transparent and transferable to other regions. Within Bavaria, the workflow can largely be adapted by changing data paths and input datasets. For other regions, transferability depends on the availability and quality of equivalent geodata and meteorological data.

The quality of the results is primarily determined by the input data and methodological assumptions. The LiDAR data used in this study represent the building stock at the time of *Airborne Laser Scanning* (ALS) and therefore do not capture later modifications. In addition, the segmentation of homogeneous roof sub-areas depends on predefined thresholds. Small roof obstacles such as skylights or chimneys are not always detected reliably, which can result in an overestimation of usable module area. Nevertheless, the results indicate that the derived roof segments provide a suitable basis for urban-scale PV potential assessment. Further uncertainties arise from the irradiation and yield modelling. Although relevant parameters such as albedo, Linke turbidity, clear-sky coefficients and temperature effects are included, the temporal resolution of the meteorological input data remains limited. As a result, short-term weather fluctuations cannot be fully represented. The use of standard values for module efficiency, performance ratio and system losses also limits the accuracy at the individual-building level. However, the calculated yields are within plausible ranges compared with reference values, indicating that the approach is appropriate for strategic assessments.

From an urban planning perspective, the priority score provides a useful first screening of suitable roof areas. It combines PV-related indicators with planning-relevant information and can support municipal PV expansion strategies. The score is based on model assumptions and does not include all implementation constraints, such as structural capacity, economic feasibility or grid connection conditions. These factors should be considered in subsequent planning steps.

5. Conclusion

This paper presents an open-source GIS-based solar cadastre implemented entirely in *QGIS* using publicly available geodata. The workflow covers the complete processing chain from LiDAR point clouds to a planner-ready priority score map and integrates roof segmentation, irradiation modelling, PV yield estimation, module coverage factors and multi-criteria prioritisation.

Applied to a $1\,\mathrm{km}^2$ case study area in *Nuremberg*, the methodology identified 3,179 technically suitable roof segments out of 241,628 analysed segments. The calculated annual yields range from $132.21\,\mathrm{kW\,h/(m^2\,a)}$ to $178.80\,\mathrm{kW\,h/(m^2\,a)}$, while the module coverage factors range from 0.383 to 0.453.

Future work should focus on the integration of economic indicators and permitting-related criteria to further increase the practical value of the cadastre for municipal planning authorities.

6. AI Statement

The authors used OpenAI's ChatGPT for language editing and the refinement of selected text passages, as well as to support the development of Python-based automation scripts. All AI-assisted content and code were critically reviewed, tested, and revised by the authors as appropriate.

7. References

Adjiski, V., Kaplan, G., Mijalkovski, S., 2023. Assessment of the solar energy potential of rooftops using LiDAR datasets and GIS based approach. International Journal of Engineering and Geosciences 8, 188–199. doi:10.26833/ijeg.1112274.

Anderegg, D., Strebel, S., Rohrer, J., 2022. Photovoltaik Potenzial auf Dachflächen in der Schweiz. Technical Report. ZHAW Zürcher Hochschule für Angewandte Wissenschaften. Wädenswil. doi:10.21256/ZHAW-2425.

Bani Salim, M., Demirocak, D.E., Barakat, N., 2018. A fuzzy based model for standardized sustainability assessment of photovoltaic cells. Sustainability 10, 4787. doi:10.3390/su10124787.

Bayerisches Landesamt für Umwelt, 2025. Energie-Atlas Bayern: Bestand Photovoltaikanlagen. Available at: https://www.karten.energieatlas.bayern.de/start/?c=651904,5477809&z=14.143&r=0&l=vt_standard,7bbee3ee-89f6-4a2e-ad96-ec1264420814&comp=recherche&research_theme=photovoltaikanlagen&tid=share&mid=1 (accessed 20 January 2026).

Bieda, A., Cienciała, A., 2021. Towards a renewable energy source cadastre—a review of examples from around the world. Energies 14, 8095. doi:10.3390/en14238095.

Cenky, M., Bendik, J., Janiga, P., Lazarenko, I., 2024. Urban-scale rooftop photovoltaic potential estimation using open-source software and public GIS datasets. Smart Cities 7, 3962–3982. doi:10.3390/smartcities7060153.

DIN Deutsches Institut für Normung e.V., 2024. DIN EN 1991-1-4:2024-03, Eurocode 1 – Einwirkungen auf Tragwerke – Teil 1-4: Windlasten; Deutsche und Englische Fassung prEN 1991-1-4:2024. Norm-Entwurf. doi:10.31030/3522290.

DWD Climate Data Center (CDC), 2024. Tägliche Stationsbeobachtungen (Temperatur, Druck, Niederschlag, Sonnenscheindauer, etc.) für Deutschland, Version v24.3. Available at: https://opendata.dwd.de/climate_environment/CDC/observations_germany/climate/daily/kl/BESCHREIBUNG_obsgermany-climate-daily-kl_de.pdf (accessed 20 January 2026).

DWD Climate Data Center (CDC), 2025a. Gridded monthly sums of incoming diffuse radiation on the horizontal plane for Germany based on ground and satellite measurements, Version V003. Available at: https://opendata.dwd.de/climate_environment/CDC/grids_germany/monthly/radiation_diffuse/ (accessed 20 December 2025).

DWD Climate Data Center (CDC), 2025b. Gridded monthly sums of incoming direct radiation on the horizontal plane for Germany based on ground and satellite measurements, Version V003. Available at: https://opendata.dwd.de/climate_environment/CDC/grids_germany/monthly/radiation_direct/ (accessed 20 December 2025).

EEG, 2025. German Renewable Energy Sources Act (EEG 2023), Section 4: Expansion Path. Available at: https://www.gesetze-im-internet.de/eeg_2014/__4.html (accessed 30 August 2026).

Fraunhofer-Institut für Solare Energiesysteme ISE, 2025. Nettostromerzeugung im 1. Halbjahr 2025: Solarstrom europaweit auf dem Vormarsch. Available at: https://www.ise.fraunhofer.de/de/presse-und-medien/presseinformationen/2025/nettostromerzeugung-im-1-halbjahr-2025-solarstrom-europaweit-auf-dem-vormarsch.html (accessed 10 November 2025).

GEG, 2024. German Building Energy Act, Annex 4 to Section 22(1). Available at: https://www.gesetze-im-internet.de/geg/anlage_4.html (accessed 13 August 2026).

Hofierka, J., Šúri, M., 2002. The solar radiation model for open source GIS: implementation and applications, in: Proceedings of the Open Source GIS – GRASS Users Conference 2002, Trento, Italy. pp. 1–19. 11–13 September 2002.

Hofierka, J., Suri, M., Huld, T., 2025. r.sun—solar irradiance and irradiation model. Available at: https://grass.osgeo.org/grass84/manuals/r.sun.html (accessed 13 August 2026).

Hook, S., Halverson, G., Johnson, M., Cawse-Nicholson, K., 2023. ECOSTRESS Tiled Ancillary NDVI and Albedo L2 Global 70 m V002. NASA EOSDIS Land Processes Distributed Active Archive Center. doi:10.5067/ECOSTRESS/ECO_L2T_STARS.002. available at: https://doi.org/10.5067/ECOSTRESS/ECO_L2T_STARS.002 (accessed 1 January 2026).

Hostettler, T., 2025. Statistik Sonnenenergie: Referenzjahr 2024. Technical Report. Swissolar. Prepared on behalf of the Bundesamt für Energie BFE.

Hou, X., Papachristopoulou, K., Saint-Drenan, Y.M., Kosmopoulos, P.G., Psiloglou, B.E., Kazadzis, S., 2025. Effects of clouds, aerosols and shadows on solar energy potential on urban rooftops using earth observation data and digital surface models. Applied Energy 397, 126243. doi:10.1016/j.apenergy.2025.126243.

IP SYSCON, Referat für Umwelt und Gesundheit, Stadt Nürnberg, 2023. Solar- und Gründachportal der Stadt Nürnberg. Available at: https://solar-gruendach-nuernberg.ipsyscon.de/ (accessed 13 August 2026).

Koch, H., Lechner, S., Erdmann, S., Hofmann, M., 2022. Assessing the potential of rooftop photovoltaics by processing high-resolution irradiation data, as applied to Giessen, Germany. Energies 15, 6991. doi:10.3390/en15196991.

Landesamt für Natur, Umwelt und Verbraucherschutz Nordrhein-Westfalen, 2013. Potenzialstudie Erneuerbare Energien NRW, Teil 2 – Solarenergie. Technical Report 40. LANUV NRW.

Ludwig, D., 2015. Methodenentwicklung zur GIS-gestützten Standortanalyse von Solaranlagen auf Grundlage hochauflösender Laserscandaten. Ph.D. thesis. Universität Osnabrück.

McGhee, R., Clarke, J.A., Svehla, K., 2024. Development and application of an urban solar photovoltaic opportunity mapping tool. Heliyon 10, e32123. doi:10.1016/j.heliyon.2024.e32123.

OpenGIS4ET Team, 2025. Citiwatts. Available at: https://www.citiwatts.eu/ (accessed 16 January 2026).

Philipps, S., Warmuth, W., 2025. Photovoltaics Report. Technical Report. Fraunhofer ISE. Version dated October 2025.

Püschel, A., 2025. Das Strahlungsjahr 2024. Technical Report. Deutscher Wetterdienst (DWD). Available at: https://www.dwd.de/DE/leistungen/solarenergie/download_strahlungsbericht_2024.pdf?__blob=publicationFile&v=1 (accessed 16 August 2026).

Sun, L., Chang, Y., Wu, Y., Sun, Y., Su, D., 2022. Potential estimation of rooftop photovoltaic with the spatialization of energy self-sufficiency in urban areas. Energy Reports 8, 3982–3994. doi:10.1016/j.egyr.2022.03.035.

Tro-Cabrera, A., Lago-Aurrekoetxea, R., Martínez-de-Alegría, I., Villamor, E., Campos-Celador, A., 2025. A methodology for assessing rooftop solar photovoltaic potential using GIS open-source software and the EROI constraint. Energy and Buildings 331, 115401. doi:10.1016/j.enbuild.2025.115401.

Uhl, J., Arnold, M., 2013. GIS-gestützter 2D-Ansatz zur Abschätzung des Photovoltaik-Potentials für großflächige Gebiete, in: Geoinformatik 2013, Heidelberg. Conference proceedings, 13–15 March 2013, Heidelberg University.

Wellner, F., Kayser, S., 2007. Grundlagen zur Erfassung der Temperaturbedingungen für eine analytische Bemessung von Asphaltbefestigungen. Technical Report FE 04.198/2004/ARB. Technische Universität Dresden. Available at: https://tu-dresden.de/bu/bauingenieurwesen/isb/strabau/ressourcen/dateien/alt/download/download-forschung/Schlussbericht04-198.pdf?lang=de (accessed 30 August 2026).

Wirth, H., 2025. Aktuelle Fakten zur Photovoltaik in Deutschland. Technical Report. Fraunhofer ISE. Version dated August 2025.